High-Temperature Materials

SCIEPublish

Article

Design of Micro/Nano-Lamellar C_4AcH_{11} and Hydrotalcite in Alumina-Spinel Castables: Enhanced High-Temperature Damage Resistance

Guoping He [1,2], Ning Liao [1,2,3,*], Wenjing Liu [1,2], Shengli Jin [1,2,3] and Yawei Li [1,2,3,*]

[1] State Key Laboratory of Advanced Refractories, Wuhan University of Science and Technology, Wuhan 430081, China; hgp20030103@163.com (G.H.); lwj04070825@163.com (W.L.); shengli.jin@wust.edu.cn (S.J.)

[2] International Joint Laboratory on New Technologies of Refractories and Metallurgy, Wuhan University of Science and Technology, Wuhan 430081, China

[3] National-Provincial Joint Engineering Research Center of High Temperature Materials and Lining Technology, Wuhan University of Science and Technology, Wuhan 430081, China

* Corresponding author. E-mail: liaoning@wust.edu.cn (N.L.); liyawei@wust.edu.cn (Y.L.)

Received: 2 June 2026; Revised: 7 July 2026; Accepted: 20 July 2026; Available online: 3 August 2026

ABSTRACT: In the present study, lamellar hydrates were designed via curing regimes and additives. Structural and high-temperature fracture behavior analyses were employed to elucidate the influence of initial lamellar hydrates on microstructural evolution and thermal stress resistance at elevated temperatures. Key findings reveal that: Pure CAC cured at 25 °C for 24 h predominantly forms metastable CAH_{10} and C_2AH_8, whereas under the two-step curing regime, the hydration products are granular C_3AH_6 and lamellar AH_3. Incorporating $CaCO_3$ and MgO under two-step curing promotes the simultaneous generation of micro/nano-lamellar C_4AcH_{11} and Mg-Al Hydrotalcite (M-A-H). The enhanced extent of hydration and pore-filling effect of M-A-H refines matrix porosity, increasing the volume fraction of 5–100 nm pores and elevating the fractal dimension (Ds). This microstructural optimization improves bonding strength, as evidenced by an 82% increase in demolding strength in the designed samples compared with the R samples. C_4AcH_{11} and M-A-H serve as reactive CaO and MgO sources, respectively, facilitating the interlocking distribution of *in-situ* CA_6 and $MgAl_2O_4$ at 1600 °C and optimizing pore structure. The hierarchical pore structure and refined crystals synergistically enhance thermal stress resistance by increasing crack deflection, dissipating energy, and improving plastic deformation capacity.

Keywords: Micron/nano lamellar hydrates; Initial hydration phases; Pore structures optimization; High-temperature fracture behavior

1. Introduction

Calcium aluminate cement (CAC)-bonded alumina-spinel castables are widely used as lining materials below the slag line in steel ladles owing to their excellent early-age bonding strength and high-temperature mechanical properties [1–3]. As a key binder phase, CAC endows the castables with performance through

a dual-action mechanism: during the curing stage, the hydrates formed via the hydration reaction create a cementitious network, providing early strength [4–7]; during high-temperature service, these hydrates gradually transform into CA_2 ($CaO·2Al_2O_3$) and CA_6, ($CaO·6Al_2O_3$) ensuring high-temperature structural stability [8–10]. Studies have shown that the microstructure of alumina-spinel castables exhibits significant inheritance, and their high-temperature performance is strongly dependent on the characteristics of the initial hydrates [11–13]. Among these, lamellar hydrates with high specific surface areas and high CaO stoichiometry (C_2AH_8 and C_4AcH_{11}, C = CaO, A = Al_2O_3, and H = H_2O) demonstrate unique advantages and will transform into interlocked or elongated CA_6 structures after high-temperature heat treatment [11,14]. Notably, as a thermodynamically stable phase, C_4AcH_{11} and its derived structures can induce the formation of a uniformly refined pore size distribution through controlled and optimized CA_6 growth. This microstructural feature effectively enhances the material's resistance to thermal shock damage through an energy dissipation mechanism, ensuring reliability during high-temperature service [14].

C_4AcH_{11} features a typical layered crystal structure, with $[Ca_4Al_2(OH)_{12}]^{2+}$ octahedral layers as the main body, which are alternately stacked with interlayer $[CO_3·3H_2O]_2^-$ units through a hydrogen bond network [15]. Guillermo et al. [16] pointed out that its formation requires three key factors: the availability of water, the carbonate content, and the ability to activate CO_3^{2-} in the system, and the avoidance of interference from monocarbonate aluminate competing phases. Based on this, the industry commonly promotes the formation of C_4AcH_{11} by introducing carbonates (e.g., calcite) into the CAC system [17–19]. This phase not only can remain stable for a long period but also retains a lamellar inherited structure when decomposed into $C_{12}A_7$ ($12CaO·7Al_2O_3$) after heat treatment at 800 °C, providing a unique structural basis for regulating high-temperature performance [20,21]. Our previous works have shown that the introduction of reactive MgO into the CAC-$CaCO_3$ system can successfully induce the formation of nano-lamellar hydrotalcite (M-A-H); Mg^{2+} reacts with $Al(OH)_4^-$/AH_3 associated with C_4AcH_{11} to form M-A-H, and its filling effect can significantly refine the pore structure of the castable. The curing regime exerts a significant influence on the stability of hydrates, the two-step curing process (40 °C × 12 h→80 °C × 12 h) can effectively induce the coexistence of micro/nano lamellar C_4AcH_{11} and M-A-H, which remarkably further enhanced the early bonding strength of the material [22]. This finding has provided a new insight into the design of high-performance castables.

However, CAC-bonded alumina-spinel castables are serviced in high-temperature environments for extended periods, where thermal stresses arising from the cyclic operation of steel ladles act as the primary driver of lining degradation. Our previous work has systematically investigated the effect of curing time on pore structure and fracture behavior [23], introduced micro/nano-lamellar C_4AcH_{11} and M-A-H hydrates into castables through two-step curing [22], and preliminarily explored the high-temperature fracture behavior of lamellar hydrate-bonded castables [24] preliminarily explored the high-temperature fracture behavior of lamellar hydrate-bonded castables. However, neither study systematically investigated how these initial hydrates affect the high-temperature performance of the castables. To date, the structural inheritance from these hydrates to high-temperature phases, their microstructural evolution at elevated temperatures, and their influence on thermal stress damage resistance remain insufficiently understood. To address this gap, the present study, building upon our previous work [22,24], focuses on: (1) systematically comparing the effects of single-step versus two-step curing on hydrate composition and morphology; (2) revealing the structural inheritance pathway from micro/nano-lamellar hydrates (C_4AcH_{11} and M-A-H) to high-temperature phases (CA_6 and $MgAl_2O_4$); (3) obtaining comprehensive quantitative fracture parameters via wedge splitting tests at 1400 °C; (4) quantitatively analyzing crack propagation paths to elucidate the energy dissipation mechanisms associated with pore refinement and *in-situ* $MgAl_2O_4$ microcrystals; and (5) introducing pore surface fractal dimension (Ds) to characterize pore structure complexity. The aim is to provide a theoretical basis and practical strategies for optimizing pore structure and high-temperature fracture behavior, thereby enhancing service reliability.

2. Materials and Methods

2.1. Preparation of Cement Hydration Samples and Alumina-Spinel Castables

Three groups of hydrated samples were prepared: R sample was pure calcium aluminate cement (CAC) cured at 25 °C for 24 h under a single-step regime; R_T sample, also pure CAC, underwent two-step curing (40 °C for 12 h followed by 80 °C for 12 h); CM_T sample, a modified CAC system with $CaCO_3$ and MgO (mass ratio CAC:$CaCO_3$:MgO = 50:10:39) from previous study, was subjected to the same two-step curing as R_T. The preparation process for all samples followed these steps: first, deionized water was added to either pure CAC powders or premixed CAC-$CaCO_3$-MgO powders, and then the mixture was made into slurry samples in Φ60 mm containers. For the two-step cured hydrated samples, the water-to-cement ratio was set to 3:1 to avoid insufficient hydration owing to excessive water loss. All slurries samples were subsequently placed in a humidity chamber and cured according to their respective regimes.

The raw materials used for the castables were tabular alumina aggregates (5–0 mm, Zhejiang Zili, Shaoxing, China), tabular alumina powder (<75 μm, Zhejiang Zili, Shaoxing, China), α-Al_2O_3 powder (~5 μm, Kaifeng Tenai, Kaifeng, China), spinel powder (<45 μm, Almatis, Qingdao, China), CAC binder (Secar 71, <45 μm, Imerys Aluminates, Tianjin, China), nano $CaCO_3$ (Shandong Jinrunze New Material, Zibo, China), and MgO (<13 μm, Qinghai Punai High-tech Materials Co., Ltd., Haidong, China), the specific compositions are referred to Table 1. The detailed preparation process of the castables is described as follows: To optimize the distribution of $CaCO_3$ and MgO around CAC, the powders were first premixed in an Eirich mixer at 2500 rpm for 15 min. Aggregates and matrices were then dry mixed for 3 min, followed by water addition and another 3 min of mixing. The wet mixture was cast into molds (40 mm × 40 mm × 160 mm and 100 mm × 100 mm × 75 mm) and vibrated for 45 s. The R samples were cured at 25 °C for 24 h, while the R_T an $C1M1_T$ samples underwent two-step curing (40 °C × 12 h → 80 °C × 12 h) to promote micro/nano-lamellar C_4AcH_{11} and M-A-H formation, providing superior early strength (demolding strength 12.0 MPa, 82% higher than R) and refined pore structure. All samples were dried at 110 °C for 24 h and fired at 1600 °C for 3 h (heating rate 5 °C/min). The water-to-cement ratio for hydration samples was 3:1, and the water addition for castables was 4.8 wt.%. This curing regime is readily implementable in existing industrial facilities.

Table 1. Batch compositions of alumina-spinel castables (wt.%).

Raw Materials		R	R_T	$C1M1_T$
Tabular alumina	5–0 mm	74	74	74
Spinel	<45 μm	15	15	15
Reactive alumina	~5 μm	6	6	6
CAC	<45 μm	5	5	5
Nano-sized $CaCO_3$		-	-	+1
MgO	<13 μm	-	-	+1
Dispersant	FS65	+0.1	+0.1	+0.1
water		+4.5	+4.5	+4.8
Curing regime		25 °C × 24 h	40 °C × 12 h→80 °C × 12 h	

+ denotes: additionally added.

2.2. Test and Characterization

It should be noted that the R sample data were reproduced under identical raw material batches and experimental conditions to those used in the present study for the R_T and $C1M1_T$ samples, ensuring comparability and minimizing potential batch-to-batch systematic errors [23,24]. The phase compositions were identified by powder X-ray diffraction analysis using a Philips X' Pert PRO diffractometer (5–90°, X' Pert PRO, PHILIPS, Amsterdam, The Netherlands). The XRD spectra were recorded at 40 mA and 40 kV

using Cu Kα radiation (λ = 0.1542 nm), with a scan rate of 10°/min and a step size of 0.05°. Microstructural observations were conducted using a scanning electron microscope (SEM, EVO10, 10 kV, Carl Zeiss, Oberkochen, Germany). Apparent porosity (AP) and bulk density (BD) were determined via the Archimedes method using water. Mercury intrusion porosimetry (MIP, AUTOPORE 9500, McMurritik Instruments, Norcross, GA, USA) was performed on 5 mm × 5 mm ×5 mm cubes extracted from the center of the castables to test the pore size distribution. In addition, the surface fractal dimension Ds was calculated to characterize the complexity of the pore structure (Equation (1))[25–27]:

$$ln\left(\frac{W_n}{r_n^2}\right) = Fd - MIP\left(ln\frac{V_n^{1/3}}{r_n}\right) + C \quad (1)$$

where W_n is the cumulative intrusion work at the n-th intrusion step, calculated as the product of the incremental mercury intrusion volume and the corresponding intrusion pressure; r_n is the pore radius corresponding to the n-th step, derived from the intrusion pressure via the Washburn equation; V_n is the cumulative mercury intrusion volume at the n-th step; D_s is the pore surface fractal dimension, which characterizes the complexity and irregularity of the pore surface (ranging from 2 for a perfectly smooth surface to 3 for an extremely rough surface); and C is a constant. The fractal dimension D_s is obtained from the slope of the linear regression of ln (W_n/r_n^2) versus ln $(V_n^{1/3}/r_n)$ [25–27].

Mechanical properties were evaluated as follows: Cold modulus of rupture (CMOR) and cold crushing strength (CCS) were measured at loading rates of 0.15 MPa/s and 1 MPa/s, respectively. The hot modulus of rupture (HMOR) of the specimens treated at 1600 °C was tested at 1400 °C, with a heating rate of 5 °C/min, a 30-min dwell time at peak temperature. High-temperature fracture behavior was assessed via wedge splitting tests (HWST) following established protocols [14]. Fracture parameters, including specific fracture energy (G_f'), nominal tensile strength (σ_{NT}), and characteristic length (l_{ch}), were calculated using Equations (2)–(6) [28,29]. And, the ratio (B+C)/A (relative crack-propagation work) quantifies crack resistance, which represents the relative crack-propagation work, where Region A corresponds to the initiation stage (from loading to peak load $F_{H,max}$), Region B to the stable propagation stage (from peak load to 50% of peak), and Region C to the unstable propagation stage (from 50% to 15% of peak). This ratio quantifies the relative distribution of fracture energy between propagation and initiation and should be interpreted alongside absolute parameters (G_f', G_f'/σ_{NT}, and l_{ch}) for a comprehensive evaluation. The definitions follow our previous methodology [14] and are consistent with wedge splitting test protocols. The fracture crack analysis was performed via SEM, and crack propagation path proportions were quantified using Image Pro Plus software (v6.0.0.260 for windows 2000/XP professional).

$$\delta_H = 2\delta_V \tan\frac{\beta}{2} \quad (2)$$

$$F_V = 2F_H \tan\frac{\beta}{2} \quad (3)$$

$$G_f{}' = \frac{1}{A}\int_0^{\delta ult} F_H d\delta_H \quad (4)$$

$$\sigma_{NT} = \frac{F_H max}{bh}\left(1 + \frac{6y}{h}\right) \quad (5)$$

$$l_{ch} = \frac{G_f{}' \cdot E}{\sigma_{NT}{}^2} \quad (6)$$

where β denotes the wedge angle (10°), δult the ultimate horizontal displacement, and A the projected area of the fracture surface. G_f' was calculated up to the point where residual force dropped to 15% of the

maximum force. Additionally, *b* and *h* represent the width and height of the fracture surface, respectively; *y* is the vertical distance from the horizontal force to the center of gravity of the fracture surface; and *E* is the elastic modulus at the tested temperature.

3. Results and Discussion

3.1. Hydrates Design Based on Simulation and Experiment

The GEMS software (v3.11.3 for windows) was employed to predict the thermodynamically stable hydrate compositions of pure CAC and CAC with $CaCO_3$ and MgO additions, as shown in Figure 1a. For pure CAC (R and R_T samples), the final hydrates stably existed as C_3AH_6 and AH_3. In contrast, upon the introduction of $CaCO_3$ and MgO into CAC, the hydrates transformed into C_4AcH_{11} and M-A-H. This was attributed to the consumption of $Al(OH)_4^-$ in the system during the formation of C_4AcH_{11} and M-A-H, resulting in a significant reduction in the content of AH_3 [30]. Further XRD analysis was conducted to determine the phase compositions of the hydrated samples, with results presented in Figure 1b. After curing at 25 °C for 24 h, the hydrates of the R sample were mainly CAH_{10} and C_2AH_8. The continuous consumption of Ca^{2+} during hydration promotes the formation of AH_3. Owing to the relatively low hydration degree at this temperature, diffraction peaks of CA and CA_2 were still detectable. For pure CAC subjected to two-step curing (R_T sample), the increased hydration temperature not only induced the transformation of metastable hydrates to C_3AH_6 and AH_3 (consistent with the GEMS simulation results) but also significantly enhanced the hydration degree, with no CAC clinker phases (CA and CA_2) detected in the sample [31–33]. For CM_T sample, the addition of $CaCO_3$ facilitated the formation of C_4AcH_{11}, and the participation of MgO at 80 °C further promoted the generation of M-A-H, accompanied by the precipitation of a small amount of AH_3. Additionally, unreacted $CaCO_3$ and MgO are detected in the system. It should be noted that GEMS simulations predict thermodynamically stable phase assemblages at equilibrium, whereas experimental XRD results reflect actual phase compositions achieved under specific kinetic conditions (curing temperature and time). The presence of metastable CAH_{10} and C_2AH_8 in the R specimens is attributed to kinetic limitations at 25 °C. Under the two-step curing regime, the elevated temperature accelerates the transformation to thermodynamically stable C_3AH_6 and AH_3, consistent with GEMS predictions.

The microstructure of the hydrated samples was observed by SEM (as shown in Figure 2): Lamellar C_2AH_8 hydrates were clearly observed in the R sample. After two-step curing, the microstructure of R_T sample was characterized by granular C_3AH_6 wrapped in AH_3. In the CM_T sample with $CaCO_3$ and MgO additions, although the hydrates retain a lamellar morphology, the hydrates had transformed from C_2AH_8 to C_4AcH_{11}, and nano-sized lamellar M-A-H was also observed.

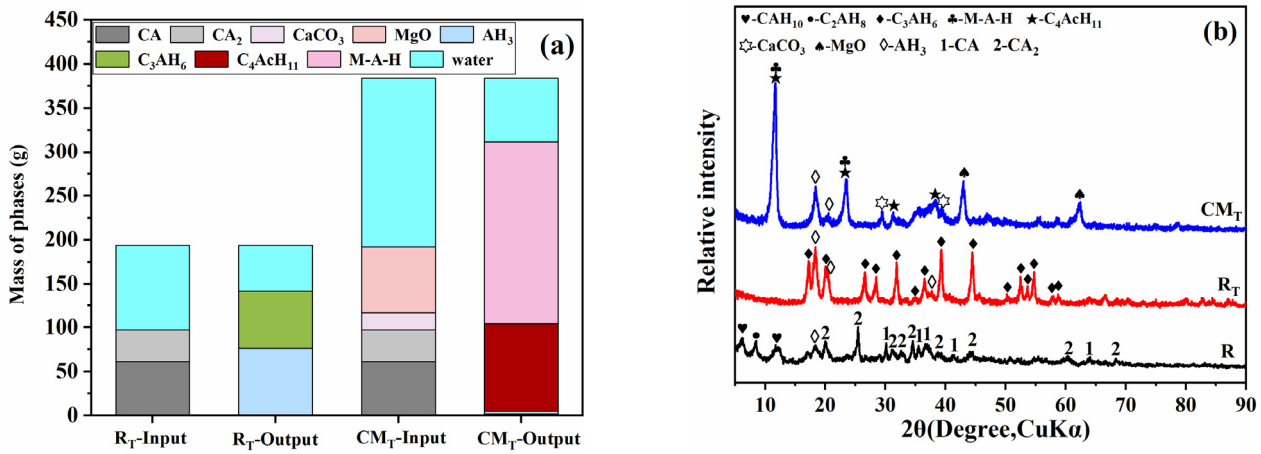

Figure 1. Simulated stable hydrates using GEMS (**a**) and experimental XRD pattern of the hydration samples (**b**).

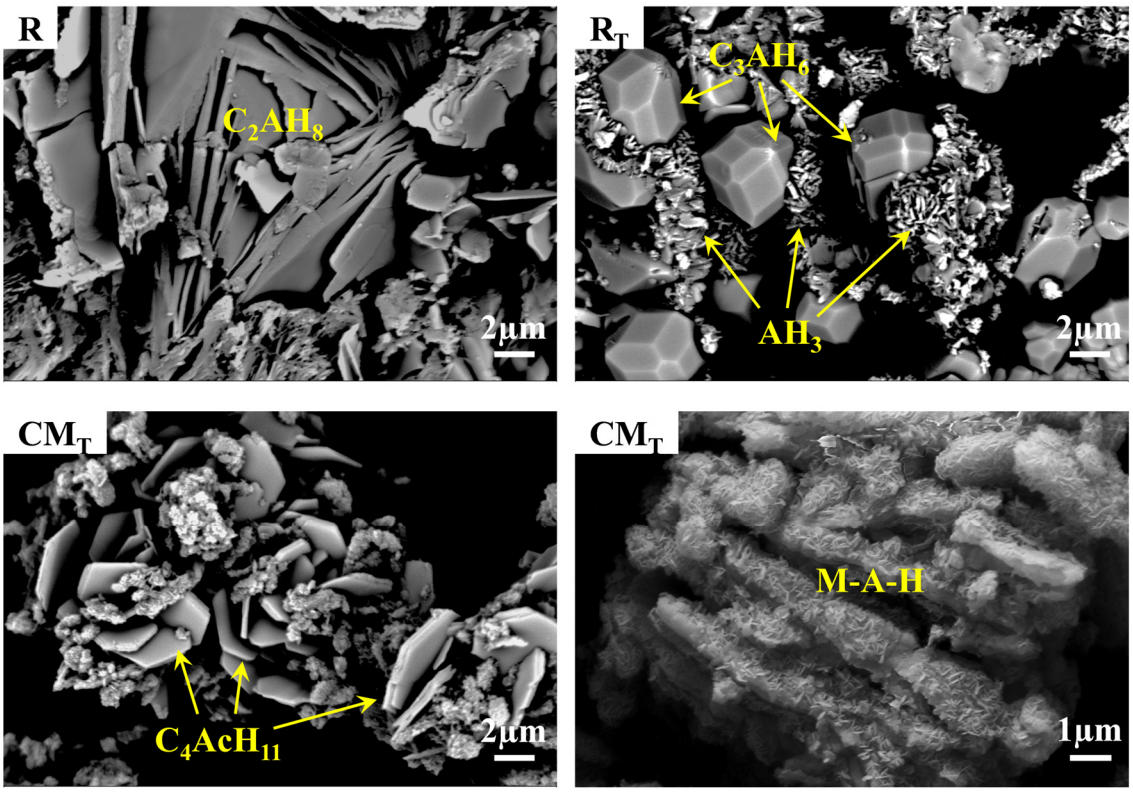

Figure 2. Microstructure of the characteristic hydrates after hydration under different conditions.

3.2. Pore Structure and Fractal Dimension of Castables

The apparent porosity and bulk density of the castables are shown in Figure 3. After curing at 25 °C, the apparent porosity of the R specimens was 9.5%, while that of the R_T specimens was approximately 7% after two-step curing, which was attributed to the enhanced degree of hydration. When micro/nano-lamellar hydrates formed in the matrix, the apparent porosity of the castables decreased significantly. This phenomenon further verified that the interlocking of nano-lamellar M-A-H within the micron-sized hydrates-C_4AcH_{11} contributed to the decreased porosity [22]. Additionally, the apparent porosity of the R specimens was significantly higher than that of other specimens, which may be attributed to its lower degree of hydration and transformation of metastable hydration phases. The decrease in apparent porosity was another reason for the increase in strength. After drying at 110 °C, the apparent porosity of the specimens was consistent with that of the green bodies the $C1M1_T$ specimens still maintained a relatively low porosity. After treatment at 1600 °C, although nano-$CaCO_3$ participated in the formation of CAC hydrates, unreacted $CaCO_3$ remained in the system. Consequently, the apparent porosity of the $C1M1_T$ specimens exceeded that of the R specimens and R_T specimens. The bulk density of the castables is illustrated in Figure 3b. The results demonstrated that the co-incorporation of nano-$CaCO_3$ and MgO into the castables slightly reduced the bulk density of the specimens.

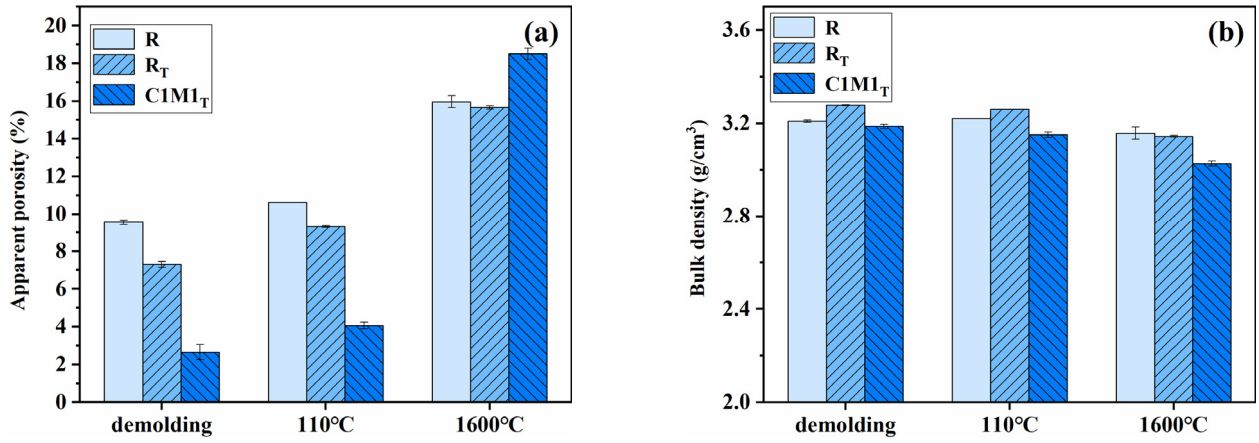

Figure 3. (**a**) Apparent porosity (AP) and (**b**) bulk density (BD) of alumina-spinel castables (R sample data are from our previous studies [23,24]).

To further investigate the pore characteristics, mercury intrusion porosimetry (MIP) was employed to analyze the pore size distribution of samples treated at 110 °C and 1600 °C, as shown in Figure 4 and Figure 5, respectively. After drying at 110 °C, both the R-110 samples and R_T-110 samples exhibited a bimodal pore distribution, with dominant peaks in the 10–200 nm and 200–2000 nm ranges. Additionally, macropores larger than 200,000 nm were detected. In contrast, the R-110 samples showed a reduced distribution in the 200–2000 nm range and a smaller average pore diameter (D_{Ave}). In contrast, the $C1M1_T$-110 samples (with co-incorporated nano-$CaCO_3$ and MgO) displayed a unimodal pore distribution, with pores concentrated in the 10–300 nm range and a smallest average pore diameter of 119 nm. Notably, large pores (>200,000 nm) were also observed in this system. Analysis of cumulative mercury intrusion curves (Figure 4b) revealed distinct differences in pore size dominance. Compared to R-110 samples and R_T-110 samples. The $C1M1_T$-110 samples exhibited a steeper slope in the <300 nm range. This steeper slope indicates a higher proportion of pores within this size range, as the slope magnitude directly correlates with pore volume concentration at specific sizes.

Furthermore, the pore size distribution across different ranges was quantified for the samples, as shown in Figure 4c. Significant differences in pore size distribution were observed among the R samples under different curing regimes. The two-step cured R_T-110 sample exhibited a dramatic proportion of pores in the 5–1000 nm range, with a 5–100 nm pore fraction of ~0.17 ± 0.01 and a 100–1000 nm pore fraction of 0.56 ± 0.03. In contrast, the $C1M1_T$-110 samples demonstrated a significant increase in the 5–100 nm pore fraction (0.44 ± 0.03) and a marked decrease in the 100–1000 nm pore fraction (0.23 ± 0.02). The development of micro/nano-structured hydrates facilitated pore refinement, reducing the average pore diameter from 555 nm to 119 nm and transforming 100–1000 nm pores into 5–100 nm pores. The pore surface fractal dimension (Ds), which characterizes the complexity of the pore structure, was calculated using pore data obtained via MIP. The results showed that the pore surface fractal dimensions (Ds) of the R-110 and R_T-110 specimens were 2.792 and 2.886, respectively, after drying. In contrast, the filling effect of the micro/nano hydrates not only significantly reduced the average pore size of the specimens but also enhanced the complexity of the pores through pore structure refinement, ultimately increasing the Ds value to 2.914 ($C1M1_T$-110 samples).

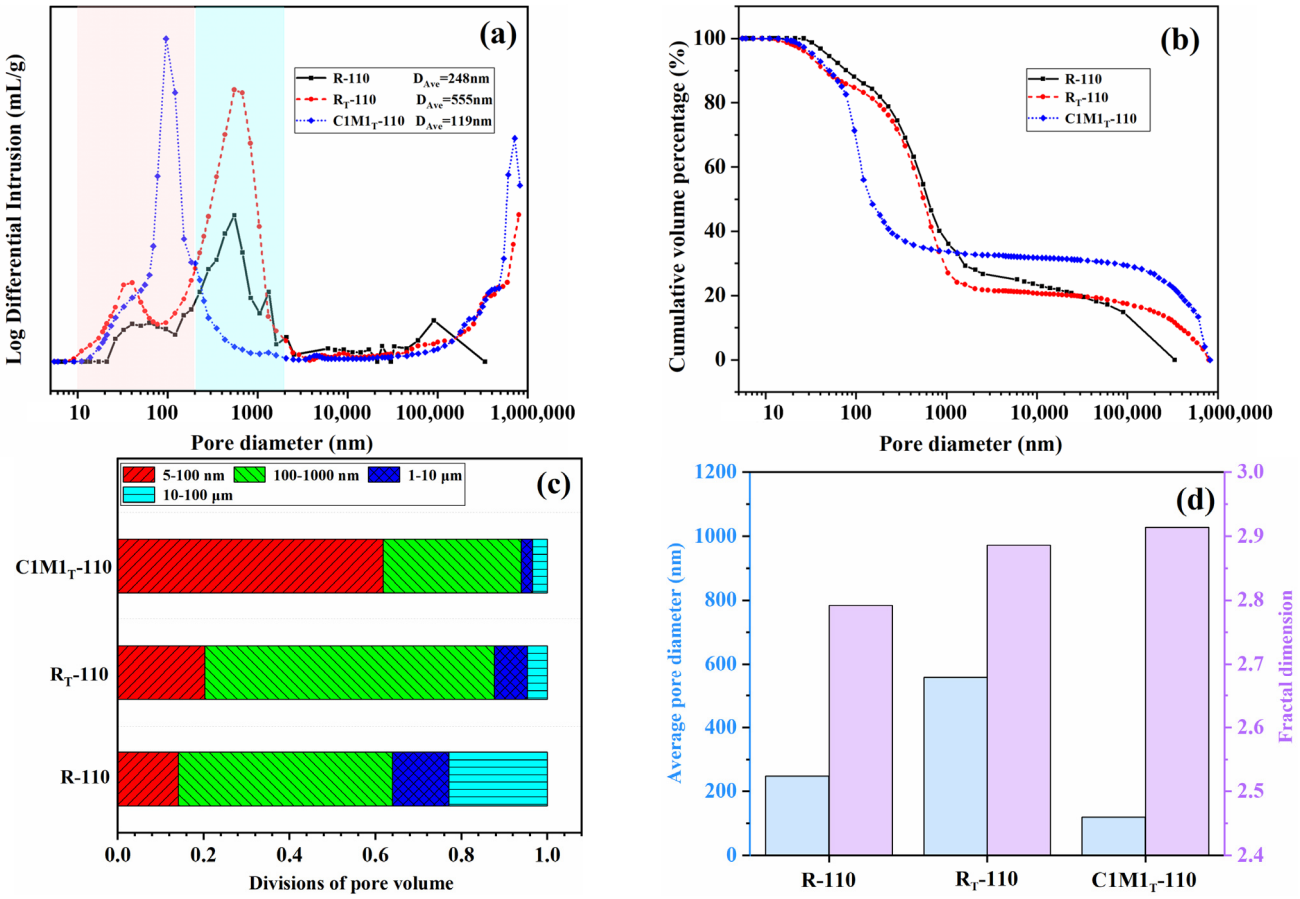

Figure 4. MIP-derived pore size distribution of castable samples dried at 110 °C: (**a**) log differential intrusion *vs.* pore diameter; (**b**) cumulative volume percentage; (**c**) volume proportion in pore size intervals; (**d**) average pore diameter [23,24]).

Similarly, the pore size distribution of specimens after 1600 °C heat treatment was analyzed to investigate the inheritance relationship between the early-stage micro/nano-layered hydrates and the pore structure evolution. Unlike samples dried at 110 °C, all 1600 °C-treated samples exhibited unimodal pore size distributions with narrower size ranges. The high-temperature sintering effect eliminated nano-sized pores, driving pore coarsening. Both the R-1600 samples and RT-1600 samples showed a broad pore size distribution (100–3000 nm), among which the R-1600 specimens had a larger average pore diameter (D_{Ave} = 1016 nm). In contrast, the C1M1T-1600 samples had a narrower distribution range (100–2000 nm) with a D_{Ave} of approximately 973 nm. As shown in Figure 5b, the C1M1T-1600 samples exhibited a steeper slope and higher cumulative mercury intrusion in the <2000 nm range. The quantification of pore fractions (Figure 5c) revealed that 1600 °C-treated samples were mainly concentrated in the 100 nm–10 μm range, with a minimal proportion of 5–100 nm pores due to the sintering effect. Given the influence of different curing regimes on the pore structure of the fired castables, the one-step cured R specimens (R-1600) had a relatively low pore fraction of 0.32 ± 0.02 in the 100–1000 nm range. In contrast, the two-step cured samples had a pore fraction of 0.45 ± 0.02 in this range, representing a 41% increase. This indicates that the enhanced degree of hydration promoted the formation of structural micro-sized pores. All specimens had a similar pore fraction of ~0.51 ± 0.04 in the 1–10 μm range. The difference was that the C1M1T-1600 specimens had a distinct advantage in the 10–100 μm range.

Compared with the dried samples, the pores of the samples after heat treatment at 1600 °C were coarsened, with the average pore diameter of all samples significantly increasing to ~1000 nm and the pore surface fractal dimension (Ds) decreasing to 2.619–2.761. This is because nano-scale and submicron-scale pores gradually disappear during the high-temperature sintering of the matrix, resulting in a reduction in the surface complexity of the pores. A comparison of the Ds values between the R samples and the C1M1T

samples showed that the inherited structure of the early micro/nano-lamellar hydrates, together with the structure of *in-situ* $MgAl_2O_4$ microcrystals embedded in the CA_6 matrix, synergistically contributes to enhancing the complexity of the pores, which will be discussed in the following section.

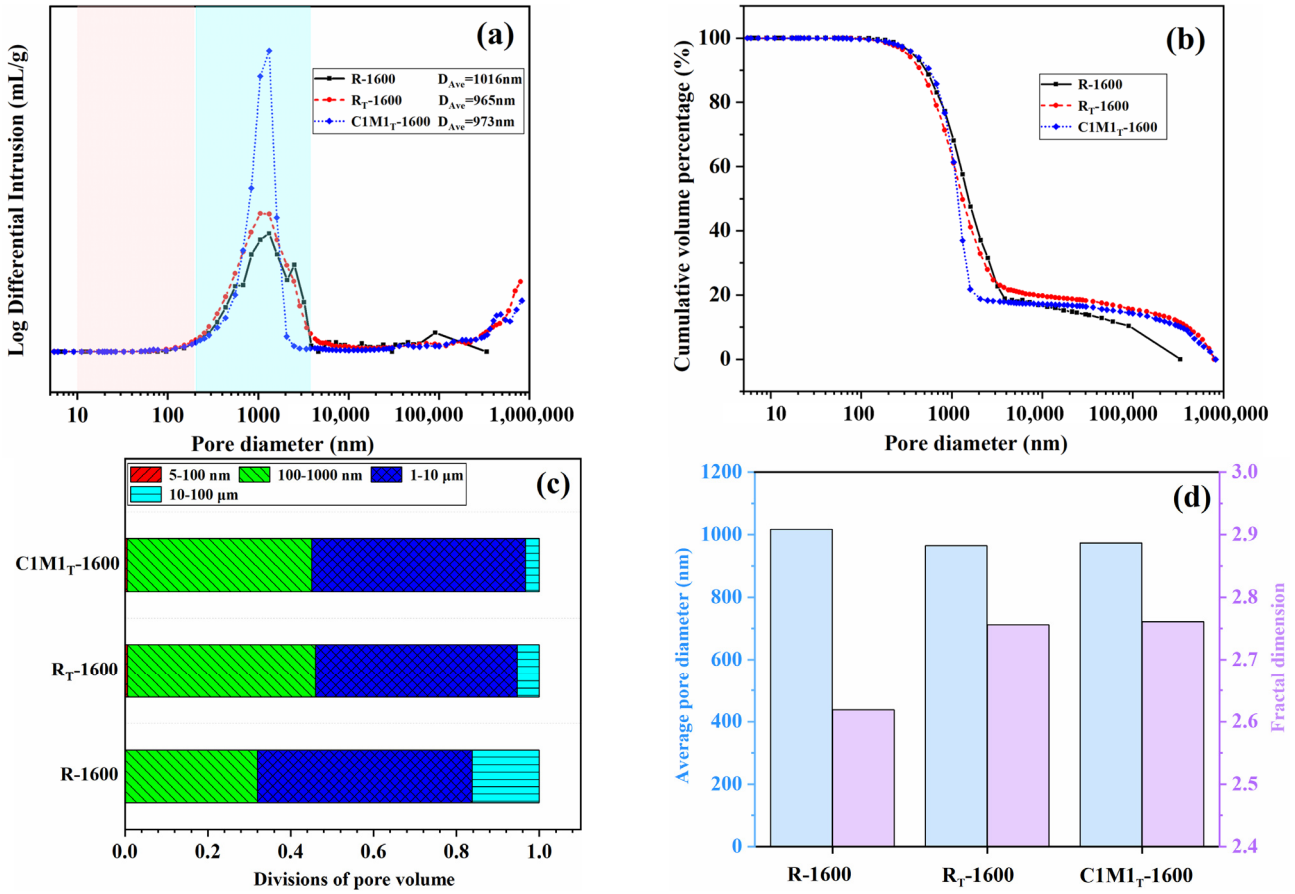

Figure 5. MIP pore structure characterization of castable samples treated at 1600 °C (R sample data are from our previous studies [23,24]). (**a**) Differential pore size distribution curves and D50 values of the samples; (**b**) Cumulative volume percentage versus pore diameter; (**c**) Volume fractions of pores in different size ranges (**d**) Average pore diameter and fractal dimension of the samples.

The above results indicate that the co-incorporation of nano-$CaCO_3$ and MgO influences CAC hydration, thereby affecting the bonding strength and pore structure of the castables. SEM analysis of the 1600 °C-treated samples (Figure 6) reveals strong aggregate-matrix bonding in all specimens, but with distinct pore characteristics. Quantitative assessment at the same scale (50 μm) shows that the R specimen has the coarsest pores (up to ~50 μm), the R_T specimen shows intermediate sizes (30–40 μm), and the $C1M1_T$ specimen exhibits the finest pore structure (mostly <25 μm). This refinement is attributed to the early-stage filling effect of M-A-H and the subsequent formation of an interlocked CA_6-$MgAl_2O_4$ structure at high temperatures, consistent with MIP results.

Combined morphological observation and XRD analysis confirm that MgO and its precursor M-A-H react with Al_2O_3 to form *in-situ* $MgAl_2O_4$ (~1–2 μm) [24], which is embedded between the lamellar CA_6 plates in the $C1M1_T$ sample, resulting in a mosaic-like microstructure. In contrast, the R and R_T samples consist predominantly of interlocking CA_6 crystals without such microcrystalline inclusions. This microstructural difference underpins the superior fracture performance of the $C1M1_T$ specimen, despite its slightly higher porosity.

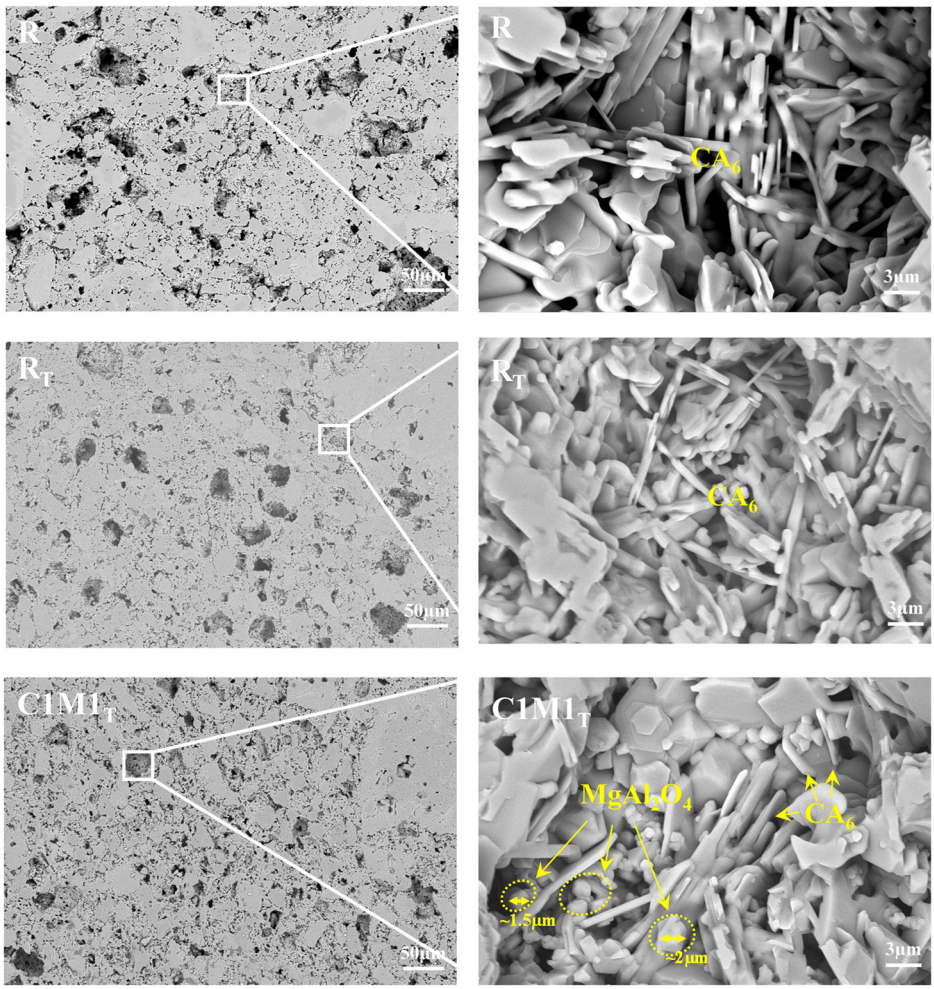

Figure 6. Microstructure of castables after 1600 °C: (**left**) matrix-aggregate interface; (**right**) magnified view of boxed region, showing interlocking CA_6 plates with *in-situ* $MgAl_2O_4$ microcrystals (~1–2 μm, arrows).

The aforementioned results demonstrated that hydrates with distinct morphologies formed during the curing process exhibited markedly different pore-structuring capabilities. After curing at 25 °C, the initial hydrates were CAH_{10} and C_2AH_8, which then transferred to C_3AH_6 and AH_3. During the two-step curing process, a higher degree of hydration and granular hydrates (C_3AH_6) preferentially facilitated the formation of 50–1000 nm pores, whereas micro/nano-lamellar hydrates (C_4AcH_{11} and M-A-H) predominantly contributed to 5–100 nm pores. These findings further validated that nano-sized M-A-H exhibits superior pore-filling efficiency, serving as the key factor in reducing open porosity and average pore diameter, refining the pore size distribution, and increasing the pore fractal dimension.

After 1600 °C heat treatment, the matrices of both the R and R_T samples primarily consisted of plate-like CA_6 and Al_2O_3 fines. In contrast, the co-incorporation of nano-$CaCO_3$ and MgO in the $C1M1_T$ samples induced the following phase-evolution pathways: Hydrate-C_4AcH_{11} and unreacted $CaCO_3$ acted as highly reactive CaO sources, reacting with Al_2O_3 to generate plate-like CA_6; The MgO precursor M-A-H and residual MgO reacted with Al_2O_3 to form *in-situ* $MgAl_2O_4$ spinel microcrystals. Owing to the 1–2 μm grain size of the $MgAl_2O_4$ microcrystals, the $C1M1_T$ samples developed a higher proportion of 100–1000 nm pores. Concurrently, the interlocking stacking of CA_6 plates promoted the formation of 1–10 μm pores, ultimately forming a more complex and refined pore structure. In summary, while the co-incorporation strategy achieved pore refinement in both dried and high-temperature-treated samples, the underlying mechanisms diverged: Refinement originated from nanoscale filling effects of M-A-H of the castables after

drying; Pore refinement stems from stacked via *in-situ* microcrystalline $MgAl_2O_4$ formation refinement arose from aggregated $MgAl_2O_4$ microcrystals stacking.

3.3. Mechanical Properties of Castables

To investigate the effect of aforementioned structure on the mechanical properties, CMOR and CCS of the castables with and without nano-sized $CaCO_3$ and MgO with different curing regimes were tested. After curing at 25 °C, the CMOR of the R specimens was 6.6 MPa. After the two-step curing, the demolding flexural strength of the R_T specimens was 8.5 MPa, while the demolding strength of the $C1M1_T$ specimens increased to 12.0 MPa, which was 82% and 41% higher compared to the R and R_T specimens, respectively. The difference in early-stage bonding strength was attributed to the degree of CAC and the type of hydrates. The R specimens exhibited low hydration degree, and their hydrates were CAH_{10} and C_2AH_8. After two-step curing, the hydration degree of CAC was increased, and the bonding phase of the R_T specimens was granular C_3AH_6 and AH_3, whereas the bonding phase of the $C1M1_T$ specimens was micro/nano-lamellar C_4AcH_{11} and M-A-H when nano-$CaCO_3$ and MgO were introduced. After drying at 110 °C, the hardening of the hydrates further improved the CMOR of the castables, and the CMOR of the $C1M1_T$ specimens was higher than that of the R specimens and R_T specimens. Upon firing at 1600 °C, the CMOR of the castables increased to more than 35 MPa owing to the formation of CA_6 lamellar interlocking structure in the specimens and the sintering effect of the matrices. However, the CMOR of the $C1M1_T$ specimens was slightly lower than that of the R specimens and R_T specimens, it can be attributed to two main factors: (1) decomposition of residual $CaCO_3$, generating additional porosity; (2) volume expansion (~5–8%) associated with *in-situ* $MgAl_2O_4$ formation, introducing microstructural stresses. CCS showed a similar trend (Figure 7b).

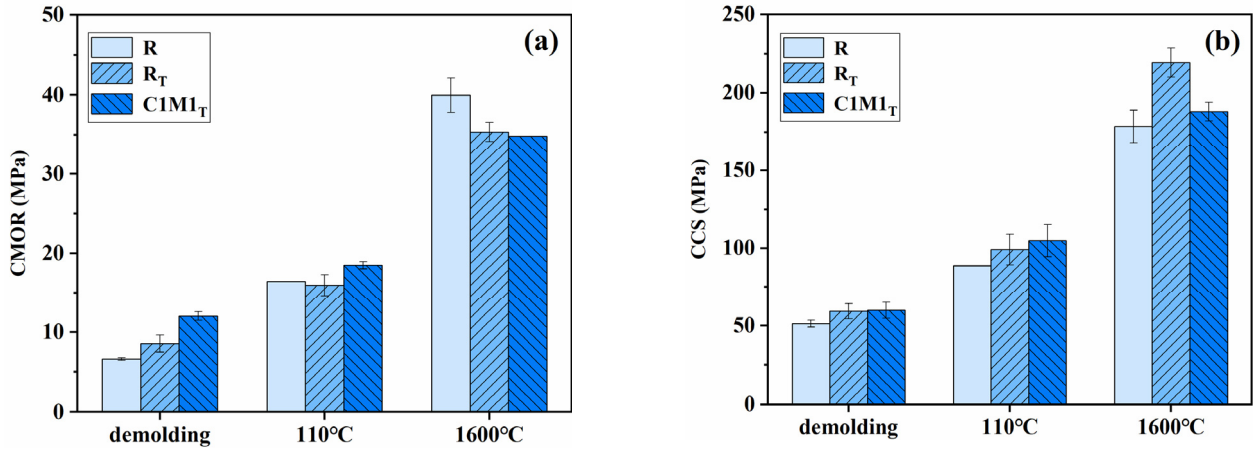

Figure 7. Mechanical properties of the castables after treatment at different temperatures: (**a**) CMOR; (**b**) CCS.

3.4. High-Temperature Thermomechanical Stress Damage Mechanisms

The high-temperature modulus of rupture (HMOR) of the castable specimens was tested at 1400 °C. The results (Figure 8) showed that all specimens exhibited HMOR values exceeding 35 MPa, which was similar to the trend of the CMOR. However, the $C1M1_T$ specimens exhibited a slight reduction in strength compared to the specimens without additives, primarily attributed to decomposition-induced pores in their microstructure.

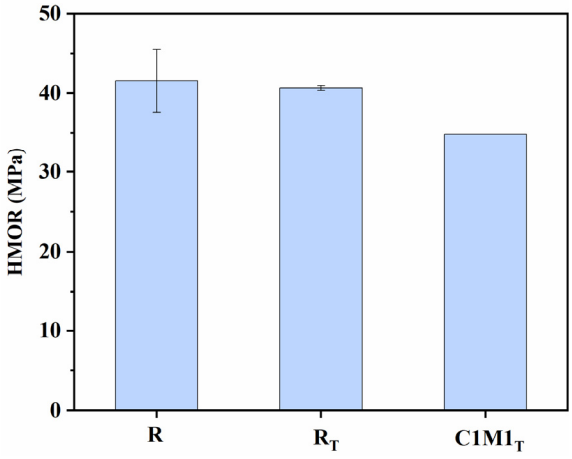

Figure 8. HMOR of alumina-spinel castables evaluated at 1400 °C.

High-temperature wedge splitting tests were conducted to characterize the thermomechanical stress damage resistance mechanism of two-step cured castables. The horizontal load-displacement curves are presented in Figure 9a, and a physical photograph of the specimens after testing is shown in Figure 9b. Upon loading, all specimens rapidly reached their maximum horizontal load ($F_{H,max}$). Although the R specimens cured at 25 °C exhibited the highest high-temperature modulus of rupture (HMOR), it had the lowest $F_{H,max}$ of approximately 3000 N, which may be related to the presence of more 10–100 μm pores. In contrast, the R_T specimen exhibited a slightly higher $F_{H,max}$ than the $C1M1_T$ specimen, consistent with their high-temperature modulus of rupture (HMOR) trends. Following peak load, a gradual load reduction phase was observed: the horizontal displacement of the R specimen was only 0.7 mm, that of the two-step cured R_T specimen was approximately 1.1 mm, and that of the $C1M1_T$ specimen significantly increased to 1.6 mm. These results indicate that the two-step cured specimens exhibit better resistance to crack propagation, and in particular, the $C1M1_T$ specimen showing superior thermal stress damage resistance.

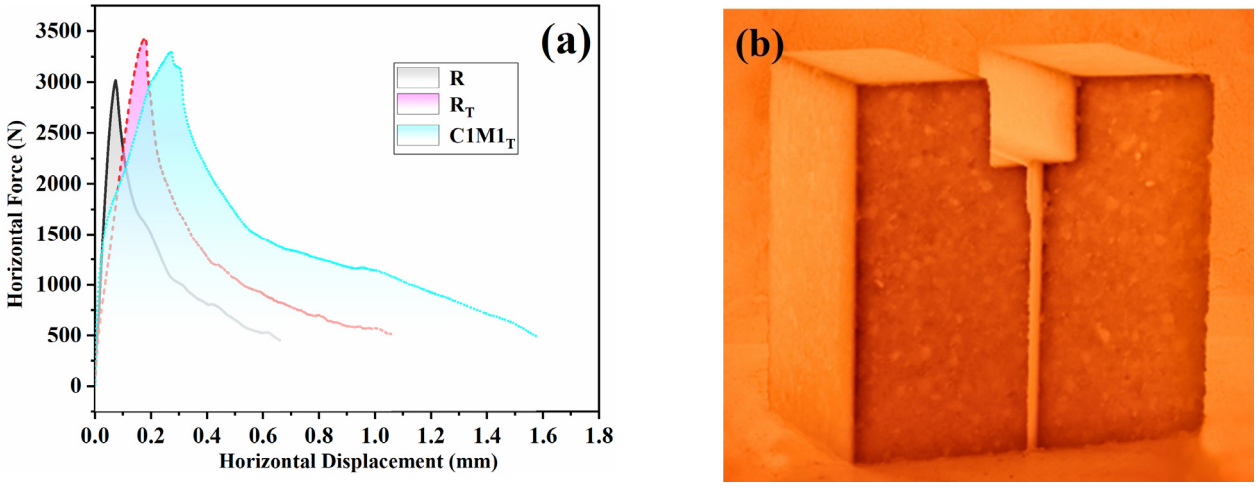

Figure 9. Horizontal force-displacement curves (**a**) and physical photo (**b**) of alumina-spinel castables evaluated at 1400 °C.

The fracture parameters derived from the horizontal load-displacement curve, including specific fracture energy (G_f'), apparent notched tensile strength (σ_{NT}), the ratio G_f'/σ_{NT}, characteristic length (l_{ch}), and the ((B+C)/A) index, were summarized in Table 2. σ_{NT}, which correlates with the maximum horizontal load ($F_{H,max}$), was slightly lower in the $C1M1_T$ specimen than in the additive-free specimen, primarily due to its higher porosity. In terms of specific fracture energy (G_f'), the R specimen cured conventionally at 25 °C exhibited a baseline value of 181.5 J/m^2. Two-step curing significantly enhanced G_f' by 74–163%: the R_T specimen reached 315.8 J/m^2, while the $C1M1_T$ specimen achieved 476.6 J/m^2. This increase

indicated that the C1M1$_T$ specimen dissipated more energy during damage, thereby suppressing the formation of new fracture surfaces. Similarly, G_f'/σ_{NT} and l_{ch} are key indicators of material toughness, with larger values signifying superior resistance to crack propagation and enhanced toughness [34,35]. The R specimen showed G_f'/σ_{NT} and l_{ch} values of 38.3 μm and 920.8 mm, respectively, whereas the C1M1$_T$ specimen exhibited values approximately three times higher (111.0 μm and 2948.9 mm), highlighting its enhanced toughness. The superior fracture parameters of the C1M1$_T$ specimen are attributed to five mechanisms: *in-situ* $MgAl_2O_4$ microcrystals (~1–2 μm) inducing crack deflection and bridging; the highest proportion of fine pores (5–1000 nm, Ds = 2.761) providing multiple energy dissipation pathways; enhanced plastic deformation capacity; multi-scale pore structure enabling synergistic energy dissipation; and structural inheritance from initial hydrates to the high-temperature CA_6-MA interlaced phase. These mechanisms collectively explain its superior fracture toughness despite slightly lower strength. It is worth noting that the higher (B+C)/A ratio of the R specimen (7.0) compared to the C1M1$_T$ specimen (4.4) does not imply superior crack resistance. Instead, this anomaly arises because the R specimen has the lowest absolute fracture energy (G_f' = 181.5 J/m^2), which minimizes Region A (initiation work) and thus artificially inflates the ratio. Additionally, the characteristic length l_{ch} is the key indicator of thermal shock resistance, representing the critical thermal strain dimension a material can sustain before failure—higher values indicate better thermal shock damage tolerance. In contrast, the C1M1$_T$ specimen exhibits G_f', G_f'/σ_{NT}, and l_{ch} values that are 2.6, 2.9, and 3.2 times those of the R specimen, clearly demonstrating superior energy dissipation and crack resistance. Therefore, (B+C)/A should always be interpreted alongside absolute fracture parameters, rather than as a standalone indicator. In summary, despite slightly lower strength than the R and R$_T$ specimens at high temperatures, the C1M1$_T$ specimen exhibits significantly higher G_f', G_f'/σ_{NT}, l_{ch}, and superior overall fracture performance. These results collectively demonstrate enhanced resistance to crack propagation and thermal stress damage.

Table 2. Fracture parameters of alumina-spinel castables evaluated at 1400 °C.

Specimens	G_f' (J/m^2)	σ_{NT} (MPa)	G_f'/σ_{NT} (μm)	l_{ch} (mm)	(B+C)/A
R	181.5	4.7	38.3	920.8	7.0
R$_T$	315.8	5.4	58.7	1244.7	3.6
C1M1$_T$	476.6	4.3	111.0	2948.9	4.4

R sample data are from our previous studies [23,24].

The crack propagation paths are typically categorized into three types: through aggregates, along aggregate-matrix interfaces, and through the matrices. To investigate the influence of optimized energy dissipation mechanisms on fracture pathways, the cracks in the samples were observed via scanning electron microscopy (SEM), as shown in Figure 10. For clarity, cracks propagating through aggregates, along interfaces, and through the matrices were marked in red, yellow, and blue, respectively. Statistical analysis of crack paths was summarized in Table 3. Compared to sintered tabular alumina aggregates, the matrices exhibited relatively weaker bonding strength and some softening deformation capacity at high temperatures, leading to a predominance of matrix-dominated fracture paths. The R sample had narrower cracks, while the C1M1$_T$ sample demonstrated larger crack opening displacements (COD, crack widths) and greater crack tortuosity than the R$_T$ sample. An increase in COD is a key characteristic of enhanced material toughness [36,37], and its core mechanisms in improving toughness can be elaborated in three aspects: energy dissipation, inhibition of crack propagation, and enhancement of plastic deformation capacity. Specifically, a larger COD implies a broader range of plastic deformation at the crack tip, which consumes more external energy; the plastic deformation at the crack tip can reduce stress concentration through a “blunting effect”, thereby delaying crack propagation; moreover, an increase in COD is often related to the complex microstructure inside the material, and the larger opening displacement provides

sufficient physical space for crack deflection and branching, extending the crack propagation path and further increasing energy consumption, ultimately enabling the material to exhibit higher toughness.

Based on statistical results, a comparison of the proportion of crack paths between the R and R_T samples indicates that the two-step curing system, which increased the degree of early hydration, was beneficial for improving the bonding strength and increasing the proportion of aggregate-penetrating fractures. When nano-$CaCO_3$ and MgO were co-incorporated, the proportion of interface-aligned cracks increased, while the proportions of aggregate-penetrating and matrix-penetrating cracks decreased. The improved toughness originates from two key energy-dissipation mechanisms in its microstructure: (1) *In-situ* $MgAl_2O_4$ microcrystals embedded within plate-like CA_6 induce crack deflection and bridging, increasing the tortuosity of crack paths; (2) The superior fracture performance of the $C1M1_T$ specimen stems from its refined pore structure, as evidenced by the highest proportion of 5–1000 nm pores and the highest pore surface fractal dimension (Ds = 2.761) after heated. These fine pores act as energy dissipation sites during crack propagation by inducing crack deflection and branching, which increases crack path tortuosity and consumes more fracture energy. In contrast, large pores (>10 μm), which are more prevalent in the R specimen, serve as stress concentrators that facilitate crack initiation and provide preferential pathways for crack propagation.

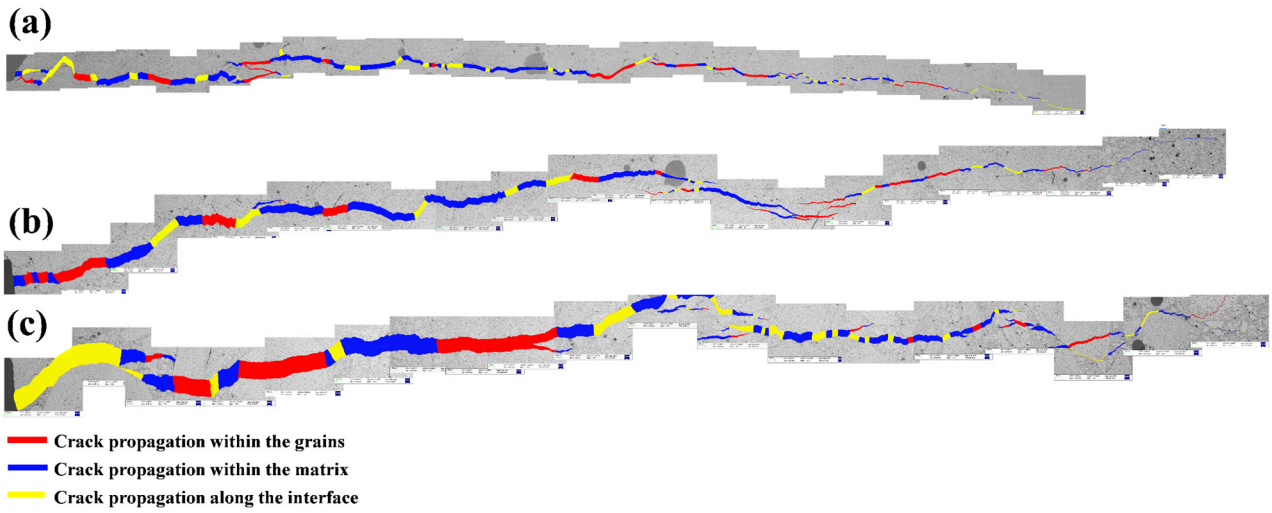

Figure 10. Pictures of crack propagation in alumina-spinel castables under SEM observation: (**a**) R; (**b**) R_T; (**c**) $C1M1_T$.

Table 3. Crack propagation path ratio of alumina-spinel castables based on SEM (%).

Index	Aggregates	Interfaces	Matrices
R	22.4	32.9	44.7
R_T	29.9	15.0	55.2
$C1M1_T$	24.4	28.0	47.6

4. Conclusions

Building upon previous research, this work comparatively investigated the effects of curing regimes and additives (nano-$CaCO_3$ and MgO) on the initial hydration phases of CAC. Furthermore, the inheritance of these microstructural features and their influence on high-temperature fracture behavior were systematically analyzed. The following conclusions are drawn:

(1) The initial hydrates of CAC were influenced by curing regimes and additives. For pure CAC, curing at 25 °C favors the formation of metastable CAH_{10} and C_2AH_8, whereas two-step curing induces the

formation of granular C_3AH_6 and AH_3. In contrast, CAC containing $CaCO_3$ and MgO promoted the generation of micro/nano-lamellar C_4AcH_{11} and M-A-H.

(2) The composite hydration phases of C_4AcH_{11} and M-A-H significantly enhanced the early bonding strength of the castables, with the demolding strength increasing by 82% and 41%, respectively, compared to the R and R_T samples. Meanwhile, the composite phases effectively refined pores, and after drying at 110 °C, the filling effect of M-A-H introduced more nano-scale pores. With C_4AcH_{11} and M-A-H serving as high-activity CaO and MgO sources, respectively, a CA_6-$MgAl_2O_4$ interlaced structure was formed after heat treatment at 1600 °C, which increased the proportion of submicron-scale pores and improved the complexity of the pore structure.

(3) A more refined and complex microporous structure was achieved through the early-stage filling effect of M-A-H and the accumulation of *in-situ* generated $MgAl_2O_4$ microcrystals. This refined CA_6-MA structure facilitates energy dissipation and crack deflection while enhancing the capacity for plastic deformation during fracture. As a result, the material exhibits significantly improved fracture toughness, with G_f' increased by 163% and l_{ch} being 3.2 times that of the R specimen, which is beneficial for extending the service life of ladle linings.

Statement of the Use of Generative AI and AI-Assisted Technologies in the Writing Process

Specifically, we have used DeepSeek (Version [DeepSeek-V3]) for English translation and language polishing during the preparation of this manuscript. All AI-generated content has been thoroughly reviewed, verified, and edited by us. We take full responsibility for the accuracy and integrity of the content.

Author Contributions

Conceptualization, Y.L. and S.J.; Methodology, N.L. and W.L.; Software, W.L.; Validation, G.H., W.L.; Formal Analysis, Y.L.; Investigation, N.L.; Resources, S.J.; Data Curation, G.H.; Writing—Original Draft Preparation, G.H.; Writing—Review & Editing, N.L.; Visualization, G.H.; Supervision, Y.L.; Project Administration, N.L.; Funding Acquisition, S.J.

Ethics Statement

Not applicable.

Informed Consent Statement

Not applicable.

Data Availability Statement

All data generated or analyzed during this study are completely presented within the published article. No external datasets were generated or deposited in public repositories, and no additional data links are required.

Funding

This research was funded by [Hubei Provincial Special Fund for Central-Guided Local S&T Development] grant number [2025CSA017]. The APC was also funded by [Hubei Provincial Special Fund for Central-Guided Local S&T Development].

Declaration of Competing Interest

The authors declare that they have no known competing financial interests or personal relationships that could have appeared to influence the work reported in this paper.

References

1. Braulio MAL, Rigaud M, Buhr A, Parr C, Pandolfelli VC. Spinel-containing alumina-based refractory castables. *Ceram. Int.* **2011**, *37*, 1705–1724. DOI:10.1016/j.ceramint.2011.03.049
2. Luz AP, Martinez AGT, Braulio MAL, Pandolfelli VC. Thermodynamic evaluation of spinel containing refractory castables corrosion by secondary metallurgy slag. *Ceram. Int.* **2011**, *37*, 1191–1201. DOI:10.1016/j.ceramint.2010.11.043
3. Samadi S, Jin S, Gruber D, Harmuth H. Thermomechanical finite element modeling of steel ladle containing alumina spinel refractory lining. *Finite Elem. Anal. Des.* **2022**, *206*, 103762. DOI:10.1016/j.finel.2022.103762
4. Braulio MAL, Morbioli GG, Milanez DH, Pandolfelli VC. Calcium aluminate cement source evaluation for Al_2O_3–MgO refractory castables. *Ceram. Int.* **2011**, *37*, 215–221. DOI:10.1016/j.ceramint.2010.09.027
5. Oliveira IR, Pandolfelli VC. Castable matrix, additives and their role on hydraulic binder hydration. *Ceram. Int.* **2009**, *35*, 1453–1460. DOI:10.1016/j.ceramint.2008.07.024
6. Idrees M, Ekincioglu O, Sonyal MS. Hydration behavior of calcium aluminate cement mortars with mineral admixtures at different curing temperatures. *Constr. Build. Mater.* **2021**, *285*, 122839. DOI:10.1016/j.conbuildmat.2021.122839
7. Ahmed AA, Shakouri M, Trejo D, Pavan Vaddey N. Effect of curing temperature and water-to-cement ratio on corrosion of steel in calcium aluminate cement concrete. *Constr. Build. Mater.* **2022**, *350*, 128875. DOI:10.1016/j.conbuildmat.2022.128875
8. Salomão R, Kawamura MA, Emilio ABV, Sakihama J, Segadães AM. Calcium aluminate cement in castable alumina: From hydrate bonding to the in situ formation of calcium hexaluminate. *Ceram. Int.* **2021**, *47*, 15082–15093. DOI:10.1016/j.ceramint.2021.02.066
9. Auvray JM, Gault C, Huger M. Evolution of elastic properties and microstructural changes versus temperature in bonding phases of alumina and alumina–magnesia refractory castables. *J. Eur. Ceram. Soc.* **2007**, *27*, 3489–3496. DOI:10.1016/j.jeurceramsoc.2007.01.016
10. Díaz LA, Torrecillas R. Phase development and high temperature deformation in high alumina refractory castables with dolomite additions. *J. Eur. Ceram. Soc.* **2007**, *27*, 67–72. DOI:10.1016/j.jeurceramsoc.2006.02.036
11. Liu W, Liao N, Nath M, Li Y, Dai Y, Pan L. Effects of characteristic hydrates on the pore structure and fracture behavior of CAC bonded alumina-spinel castables. *Constr. Build. Mater.* **2023**, *389*, 131736. DOI:10.1016/j.conbuildmat.2023.131736
12. Antonovič V, Kerienė J, Boris R, Aleknevičius M. The Effect of Temperature on the Formation of the Hydrated Calcium Aluminate Cement Structure. *Procedia Eng.* **2013**, *57*, 99–106. DOI:10.1016/j.proeng.2013.04.015
13. Liao N, Liu W, Yang J, Nath M, Dai Y, Pan L, et al. In-depth investigation of pore structure and fracture behavior of CAC bonded alumina-spinel castables treated at 110~1600 °C. *Ceram. Int.* **2022**, *48*, 33763–33772. DOI:10.1016/j.ceramint.2022.07.321
14. Liu W, Liao N, Nath M, Li Y, Dai Y, Pan L. Assessment of fracture behavior of mono-carbonate (C_4AcH_{11}) bonded alumina-spinel castables by wedge splitting test. *J. Eur. Ceram. Soc.* **2024**, *44*, 2600–2608. DOI:10.1016/j.jeurceramsoc.2023.11.011
15. Renaudin G, Francois M, Evrard O. Order and disorder in the lamellar hydrated tetracalcium monocarboaluminate compound. *Cem. Concr. Res.* **1999**, *29*, 63–69. DOI:10.1016/S0008-8846(98)00184-7
16. Puerta-Falla G, Balonis M, Le Saout G, Kumar A, Rivera M, Falzone G, et al. The influence of slightly and highly soluble carbonate salts on phase relations in hydrated calcium aluminate cements. *J. Mater. Sci.* **2016**, *51*, 6062–6074. DOI:10.1007/s10853-016-9912-9
17. Luz AP, Pandolfelli VC. $CaCO_3$ addition effect on the hydration and mechanical strength evolution of calcium aluminate cement for endodontic applications. *Ceram. Int.* **2012**, *38*, 1417–1425. DOI:10.1016/j.ceramint.2011.09.021
18. Zeng J, Liu M, Zhang Z, Mu Y, Liu C, Ye G. Influence of micro-sized $CaCO_3$ on hydrates formation of residual calcium aluminate cement in castables during drying. *Int. J. Appl. Ceram. Technol.* **2024**, *21*, 1616–1624. DOI:10.1111/ijac.14623
19. Goergens J, Manninger T, Goetz-Neunhoeffer F. *In-situ* XRD study of the temperature-dependent early hydration of calcium aluminate cement in a mix with calcite. *Cem. Concr. Res.* **2020**, *136*, 106160. DOI:10.1016/j.cemconres.2020.106160
20. Liu M, Zeng J, Jin D, Mu Y, Zhou W, Ye G. Influence of mono-carbonate hydrates on mechanical properties of CAC bonded castables fired at 800 °C. *Mater. Chem. Phys.* **2023**, *301*, 127644. DOI:10.1016/j.matchemphys.2023.127644
21. Goergens J, Goetz-Neunhoeffer F. Temperature-dependent late hydration of calcium aluminate cement in a mix with calcite—Potential of G-factor quantification combined with GEMS-predicted phase content. *Cement* **2021**, *5*, 100011. DOI:10.1016/j.cement.2021.100011

22. Liu W, Liao N, Peng H, Li Y, Yan W, Wang X, et al. Design of micron/nano-sized lamellar C(M)-A-H hydrates enhanced alumina-spinel castables through two-step curing. *Ceram. Int.* **2025**, *51*, 9852–9863. DOI:10.1016/j.ceramint.2024.12.417
23. Liu W, Liao N, Nath M, Ji Z, Dai Y, Pan L, et al. Effects of curing time on the pore structure evolution and fracture behavior of CAC bonded alumina-spinel castables. *Ceram. Int.* **2022**, *48*, 25000–25010. DOI:10.1016/j.ceramint.2022.05.153
24. Li Y, Liu W, Liao N, Nath M, Tie S, Liu X. Investigation of pore structure and high-temperature fracture behavior of lamellar hydrates bonded alumina-spinel castables. *J. Eur. Ceram. Soc.* **2024**, *44*, 5252–5261. DOI:10.1016/j.jeurceramsoc.2024.02.035
25. Zhang B, Li S. Determination of the Surface Fractal Dimension for Porous Media by Mercury Porosimetry. *Ind. Eng. Chem. Res.* **1995**, *34*, 1383–1386. DOI:10.1021/ie00043a044
26. Schmitt Rahner M, Halisch M, Peres Fernandes C, Weller A, Sampaio Santiago dos Santos V. Fractal dimensions of pore spaces in unconventional reservoir rocks using X-ray nano- and micro-computed tomography. *J. Nat. Gas Sci. Eng.* **2018**, *55*, 298–311. DOI:10.1016/j.jngse.2018.05.011
27. Zhang B, Liu W, Liu X. Scale-dependent nature of the surface fractal dimension for bi- and multi-disperse porous solids by mercury porosimetry. *Appl. Surf. Sci.* **2006**, *253*, 1349–1355. DOI:10.1016/j.apsusc.2006.02.009
28. Jin S, Gruber D, Harmuth H. Determination of Young's modulus, fracture energy and tensile strength of refractories by inverse estimation of a wedge splitting procedure. *Eng. Fract. Mech.* **2014**, *116*, 228–236. DOI:10.1016/j.engfracmech.2013.11.010
29. Ribeiro S, Rodrigues JA. The influence of microstructure on the maximum load and fracture energy of refractory castables. *Ceram. Int.* **2010**, *36*, 263–274. DOI:10.1016/j.ceramint.2009.07.033
30. Goergens J, Belli R, Schulbert C, Goetz-Neunhoeffer F. Influence of different CA_2/CA-ratios on hydration degree, AH_3 content and flexural strength investigated for a binder formulation of calcium aluminate cement with calcite. *Cem. Concr. Res.* **2023**, *165*, 107090. DOI:10.1016/j.cemconres.2023.107090
31. Li J, Chang J, Wang T, Zeng T, Li J, Zhang J. Effects of phosphogypsum on hydration properties and strength of calcium aluminate cement. *Constr. Build. Mater.* **2022**, *347*, 128398. DOI:10.1016/j.conbuildmat.2022.128398
32. Son HM, Park S, Kim HY, Seo JH, Lee HK. Effect of $CaSO_4$ on hydration and phase conversion of calcium aluminate cement. *Constr. Build. Mater.* **2019**, *224*, 40–47. DOI:10.1016/j.conbuildmat.2019.07.004
33. Son HM, Park SM, Jang JG, Lee HK. Effect of nano-silica on hydration and conversion of calcium aluminate cement. *Constr. Build. Mater.* **2018**, *169*, 819–825. DOI:10.1016/j.conbuildmat.2018.03.011
34. Harmuth H. Stability of crack propagation associated with fracture energy determined by wedge splitting specimen. *Theor. Appl. Fract. Mech.* **1995**, *23*, 103–108. DOI:10.1016/0167-8442(95)00008-3
35. Khlifi I, Pop O, Dupré JC, Doumalin P, Huger M. Investigation of microstructure-property relantionships of magnesia-hercynite refractory composites by a refined digital image correlation technique. *J. Eur. Ceram. Soc.* **2019**, *39*, 3893–3902. DOI:10.1016/j.jeurceramsoc.2019.05.010
36. Raja RB, Sivakumar MVN, Sai AP. Numerical simulation of wedge splitting test method for evaluating fracture behaviour of self compacting concrete. *Comput. Concr. Int. J.* **2024**, *33*, 265–273. DOI:10.12989/cac.2024.33.3.265
37. Brochen E, Dannert C, Paul J, Krause O. Investigation of fracture behavior of typical refractory materials up to service temperatures. *Int. J. Ceram. Eng. Sci.* **2022**, *4*, 68–76. DOI:10.1002/ces2.10123